

Instability of a plane Poiseuille flow bounded between inhomogeneous anisotropic porous layers

Supriya Karmakar^a, Priyanka Shukla^a

^a*Department of Mathematics, Indian Institute of Technology Madras, Chennai, 600036, Tamil Nadu, India*

Abstract

The linear stability analysis of a plane Poiseuille flow in a channel with anisotropic and inhomogeneous porous layers is performed. The generalized Darcy equation, along with the Navier–Stokes equation, governs the flow in the porous-fluid-porous channel. The Beaver–Joseph interface condition is assumed, which considers the coupling between the flows in the porous and fluid layers. The spectral collocation method is employed to solve the Orr–Sommerfeld type eigenvalue problem for the amplitude of the disturbances of arbitrary wavenumbers. The effect of anisotropy and inhomogeneous permeability on the stability characteristics is addressed in detail. The stability characteristics of the anisotropy parameter (the ratio of permeability in the streamwise and the transverse direction) and the inhomogeneity function are presented in detail.

Keywords: interfacial flow, permeability, anisotropy, inhomogeneity, multi-layer flow

1. Introduction

Stability analysis of the flow through multi-layer porous fluid systems is a subject that has been studied extensively for the past many decades. Various applications, ranging from geophysical, industrial, technological, and biological systems employ multi-layer porous flow systems [1–17]. For instance, the permeable coastal sediment flows, flows in fractured geological strata [8, 9, 15–17], and gas flooding by injecting CO₂ or nitrogen to enhance oil recovery from oil reservoirs [1]. The manufacturing of cost-effective composite materials by resin film infusion (RFI), where resin flows, can be described by Darcy’s law. Such composite materials are used in aircraft or motor car production [2]. Another example of multi-layer porous-fluid systems is the blood flow through arteries, the gastrointestinal system, kidneys, and lungs [10, 13, 14]. For example, the stability analysis of blood flows in a large artery, by treating the large artery as a rigid channel with uniform width and the blood as an incompressible Newtonian fluid with variable viscosity due to transverse variation in hematocrit ratio, was performed by Makinde [10]. He observed that a transverse increase in the hematocrit ratio towards the arterial central region has a stabilizing effect.

Chang et al. [18] performed the foremost stability work on a pressure-driven fluid flow overlying a saturated porous region. They numerically solved the Navier–Stokes–Darcy model and identified three different instability modes. Liu et al. [19] solved the same problem using the Brinkman model and revealed two unstable modes in contrast to Chang et al. [18]. Hill and Straughan [20] adopted a more generalized model by considering three regions in which a Darcy–Brinkman porous media is introduced between the fluid and Darcy regions. The neutral stability

curves are not found to be bimodal for specific parameter regimes. Detailed linear stability of a plane Poiseuille flow in a confined porous channel was analyzed by Tilton and Cortelezzi [21, 22] by considering the volume-averaged Navier–Stokes equations (VANS) equation [23] along with the shear stress conditions given by Ochoa-Tapia and Whitaker [24, 25]. Tilton and Cortelezzi [21, 22] suggested that inertial effects can be neglected if the ratio between the square root of permeability and channel half-height, i.e. the mean permeability, is minimal. They concluded that the small increment in wall-permeability decreases the critical Reynolds number compared to the plane Poiseuille flow between rigid walls. Some other studies reported instability mechanism of porous-fluid configuration in the presence or absence of heat transfer (see, e.g., Nield et al. [3], Straughan [26]).

In several practical situations and natural processes, a porous layer exhibits directional and spatial variation [27, 28]. Therefore, it is deemed necessary to consider the effects of anisotropy and inhomogeneity while exploring the stability characteristics of a porous-fluid system. Deepu et al. [29] analyzed the impact of anisotropic and inhomogeneous permeability on the linear stability results proposed by Chang et al. [18]. Their study reveals that a suitable wall-parallel or wall-normal permeability can control flow instability in porous channels. However, choosing the optimal model for governing porous-fluid channels remains unanswered [19].

In this regard, the main objective of the present study is to investigate the effect of anisotropic and inhomogeneous permeability on the flow instabilities in a confined porous channel in isothermal conditions by using the generalized Darcy’s equation along with the Beavers and Joseph [30] boundary condition. The paper follows the following structure. Section 2 describes the problem description and governing equations, the analytical expression of the base state solution, and the derivation of linear stability equations. The numerical method is explained in Sec. 3. The stability features for anisotropy and inhomogeneity are discussed in Sec. 4. Conclusions are in Sec. 5.

2. Mathematical formulation and governing equations

Consider a two-dimensional plane Poiseuille flow of an incompressible viscous fluid in a channel of height $2h$ bounded between two saturated porous layers of thickness $2h_1$ and $2h_2$. A constant pressure gradient drives the flow. The lengths are measured from the center line of the channel, as shown in figure 1. The governing continuity and momentum balance equations in the

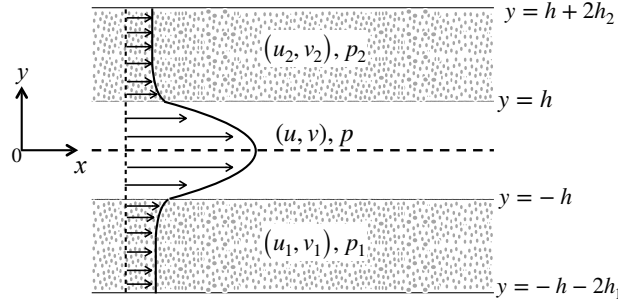


Figure 1: Schematic of a two-dimensional plane Poiseuille flow in a channel bounded between two porous layers.

fluid layer spanning $y \in (-h, h)$ read

$$\nabla \cdot \mathbf{u} = 0, \quad (2.1a)$$

$$\rho \left(\frac{\partial \mathbf{u}}{\partial t} + \mathbf{u} \cdot \nabla \mathbf{u} \right) = -\nabla p + \mu \nabla^2 \mathbf{u}, \quad (2.1b)$$

where t denotes the time, x and y are the streamwise and transverse directions, respectively, $\mathbf{u} = (u, v)$, p and μ are the velocity vector, pressure and viscosity, respectively.

We consider highly dense porous layers, i.e., the permeability is low; hence the generalized Darcy's law governs the momentum transport in the flow system [3]. The continuity and generalized Darcy equation in the porous layers spanning $y \in (-h - 2h_1, -h) \cup (h, h + 2h_2)$ read

$$\nabla \cdot \mathbf{u}_j = 0, \quad (2.2a)$$

$$\frac{\rho}{\epsilon_j} \frac{\partial \mathbf{u}_j}{\partial t} = -\nabla p_j - \frac{\mu}{\mathbf{K}} \mathbf{u}_j, \quad (2.2b)$$

where $j = 1$ and 2 denotes the lower and upper layers, respectively, ϵ_j is the porosity, $\mathbf{u}_j = (u_j, v_j)$ is the volume averaged velocity vector, and p_j is the intrinsic averaged pressure. The permeability tensor \mathbf{K} reads

$$\mathbf{K} = \begin{pmatrix} k_{jx} \eta_{jx}(y/h) & 0 \\ 0 & k_{jy} \eta_{jy}(y/h) \end{pmatrix}, \quad (2.3)$$

where k_{jx} and k_{jy} are the permeabilities in the x - and y -direction, respectively; η_{jx} and η_{jy} are the corresponding inhomogeneity functions depend only on y . The anisotropy parameter $\xi_j = k_{jx}/k_{jy}$ is defined as the ratio of the permeabilities. Note that the inhomogeneity functions η_{jx} , η_{jy} can depend on x and y both; however, this gives rise to a two-dimensional base flow, thus making the problem complicated. A linear inhomogeneity function is used by Green and Freehill [31]. However, in the present analysis, an inhomogeneous exponential function [29, 32, 33] of the following form is employed,

$$\eta_{jx} = \eta_{jy} = e^{\mathcal{I}_j(1 \mp \frac{y}{h})}, \quad (2.4)$$

where \mathcal{I}_j is the inhomogeneity factor. Note that at lower and upper porous-fluid interfaces, $\eta_{jx}(\mp h) = \eta_{jy}(\mp h) = 1$. And the permeabilities in the x - and y -directions increase (decrease) with negative (positive) values of \mathcal{I}_j for both porous layers.

No penetration conditions are applied at the bottom $y = -h - 2h_1$ ($j = 1$) and top $y = h + 2h_2$ ($j = 2$) of the porous layers,

$$v_j = 0. \quad (2.5)$$

The continuity of velocity and balance of normal and shear stresses are imposed at the interfaces, which, respectively, read

$$v = v_j, \quad p - 2\mu \frac{\partial v}{\partial y} = p_j \quad \text{and} \quad \frac{\partial u}{\partial y} = \pm \frac{\alpha_j^{BJ}}{\sqrt{k_{jx} \eta_{jx}(\mp h)}} (u - u_j), \quad (2.6 \text{ a,b,c})$$

where $\eta_{jx}(\mp h) = 1$, α_j^{BJ} denotes the Beaver–Joseph coefficient, which depends on the local structure of the porous materials near the fluid-porous interfaces [30, 34]. The positive and

negative signs in (2.6c) stand for the interface of lower and upper porous layers, respectively. Note that Beavers and Joseph [30] condition (2.6c) is employed, along with the streamwise component of permeability [32].

2.1. Dimensionless governing equations and boundary conditions

The following scaling is used for non-dimensionalization of the flow variables

$$(x^*, y^*) = \frac{1}{h}(x, y), \quad t^* = \frac{tU_m}{h}, \quad \mathbf{u}^* = \frac{\mathbf{u}}{U_m}, \quad p^* = \frac{p}{\rho U_m^2}, \quad \mathbf{u}_j^* = \frac{\mathbf{u}_j}{U_m}, \quad p_j^* = \frac{p_j}{\rho U_m^2}, \quad j = 1, 2,$$

where h is the half height of the open channel layer and U_m is the mean channel velocity. After dropping \star , the non-dimensional form of (2.1)–(2.2) is

$$\frac{\partial \mathbf{u}}{\partial t} + (\mathbf{u} \cdot \nabla) \mathbf{u} = -\nabla p + \frac{1}{Re} \nabla^2 \mathbf{u}, \quad \nabla \cdot \mathbf{u} = 0, \quad (2.7a,b)$$

$$\frac{\partial \mathbf{u}_j}{\partial t} = -\epsilon_j \nabla p_j + \frac{1}{\sigma_j^2 Re} \left(\frac{1}{\eta_{jx}(y)}, \frac{\xi_j}{\eta_{jy}(y)} \right) \odot \mathbf{u}_j, \quad \nabla \cdot \mathbf{u}_j = 0, \quad (2.8a,b)$$

where $Re = \rho U_m h / \mu$ and $\sigma_j = \sqrt{k_{jx}} / h$ are the Reynolds number and the mean permeability, respectively, and $\xi_j = k_{jx} / k_{jy}$ is the anisotropy parameter. Here, \odot represents the Hadamard product (or the element-wise product of two vectors), and the indices $j = 1$ and $j = 2$ refer to the lower $-1 - 2d_1 < y < -1$ and the upper $1 < y < 1 + 2d_2$ porous layers, respectively. $d_j = h_j / h$ is the ratio of the thickness of the j^{th} porous layer to the open channel layer. The non-dimensional interface conditions—continuity of velocity, normal and shear stresses conditions—at $y = \pm 1$ become

$$v = v_j, \quad p - \frac{2}{Re} \frac{\partial v}{\partial y} = p_j \quad \text{and} \quad \frac{\partial u}{\partial y} = \pm \frac{\alpha_j^{BJ}}{\sigma_j} \frac{1}{\sqrt{\eta_{jx}(\mp 1)}} (u - u_j), \quad (2.9a,b,c)$$

and no-penetration conditions at $y = \pm(1 + 2d_j)$ read as

$$v_j = 0. \quad (2.10)$$

2.2. Base flow

The undisturbed flow is assumed to be the steady $[\partial(\cdot)/\partial t]$ and fully developed $[\partial(\cdot)/\partial x]$ plane Poiseuille flow in both the channel and porous layers. Under these assumption solving the non-dimensionalized governing equations and boundary conditions (2.7)–(2.10), we get the base state velocity $U_B = [U_2, U, U_1]$ and pressure $[P_2, P, P_1]$ in each layer as

$$\begin{aligned} U_2(y) &= -2A\sigma_2^2\eta_{2x}(y), & 1 \leq y \leq 1 + 2d_2 \\ U(y) &= Ay^2 + By + C, & -1 \leq y \leq 1 \\ U_1(y) &= -2A\sigma_1^2\eta_{1x}(y), & -1 - 2d_1 \leq y \leq -1 \\ P(x) = P_1(x) = P_2(x) &= \frac{1}{Re} \left(\frac{1}{1/6 + C/A} \right) x + \text{contant} \end{aligned} \quad (2.11 a,b,c,d)$$

where

$$\left. \begin{aligned}
 A &= 2(1/6 - E/G), \quad B = AF/G, \quad C = AE/G, \\
 E &= \left(\frac{\alpha_1^{BJ} (\chi_1^2 \sigma_1^2 + 1)}{\chi_1 \sigma_1} + 1 \right) \left(\frac{\alpha_2^{BJ}}{\chi_2 \sigma_2} + 1 \right) + \left(\frac{\alpha_2^{BJ} (\chi_2^2 \sigma_2^2 + 1)}{\chi_2 \sigma_2} + 1 \right) \left(\frac{\alpha_1^{BJ}}{\chi_1 \sigma_1} + 1 \right), \\
 F &= \frac{\alpha_2^{BJ}}{\sigma_2 \chi_2} - \frac{\alpha_1^{BJ}}{\sigma_1 \chi_1} + \alpha_1^{BJ} \alpha_2^{BJ} \left(\frac{\chi_1 \sigma_1}{\chi_2 \sigma_2} - \frac{\chi_2 \sigma_2}{\chi_1 \sigma_1} \right), \\
 G &= \frac{\alpha_2^{BJ}}{\sigma_2 \chi_2} \left(1 + \frac{\alpha_1^{BJ}}{\sigma_1 \chi_1} \right) + \frac{\alpha_1^{BJ}}{\sigma_1 \chi_1} \left(1 + \frac{\alpha_2^{BJ}}{\sigma_2 \chi_2} \right), \\
 \eta_{jx} &= \eta_{jy} = e^{I_j(1 \mp y)}, \\
 \chi_1 &= \sqrt{\eta_{1x}(-1)} = 1, \quad \text{and} \quad \chi_2 = \sqrt{\eta_{2x}(1)} = 1.
 \end{aligned} \right\} \quad (2.12)$$

It is worth noticing that the base state velocity profile is independent of anisotropy parameter ξ_j . This is due to the fact that the y-momentum equation for the porous layer is identically satisfied under the base flow assumptions.

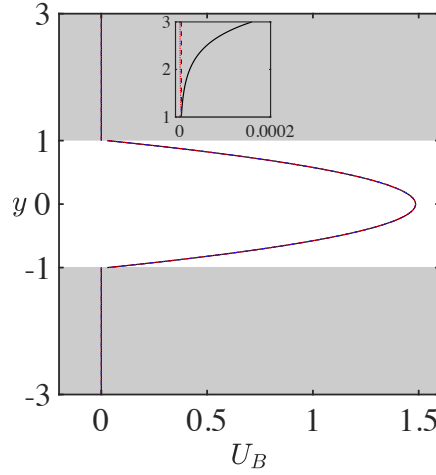


Figure 2: Base flow profile $U_B = [U_2, U, U_1]^T$ in both the open channel and porous layers for three different values of inhomogeneity factor: $I_1 = I_2 = -2$ (solid line), 0 (dashed line) and 2 (dotted line). The other parameters are fixed at $\sigma_1 = \sigma_2 = 0.001$, $\epsilon_1 = \epsilon_2 = 0.3$, $\alpha_1^{BJ} = \alpha_2^{BJ} = 0.1$. The inset shows the zoomed part in the upper porous region.

Figure 2 displays the base flow profile of identical porous layers (i.e., the mean permeability, porosity, Beaver–Joseph coefficient and inhomogeneity factor are the same in both the porous layers) for three different values of inhomogeneity factor $I_1 = I_2 = I = -2, 0$ and 2. Since all layers are of equal width $d_1 = d_2 = 1$, the velocity profile is symmetric about the center-line of the channel. A jump in the interface velocity exists for all considered inhomogeneity factors due to the choice of interface condition (2.15c) [30]. Note that for all values of inhomogeneity factor, the base flow profiles are parabolic and overlap in the open channel layer. However, the base velocity in the porous layers is uniform for the homogeneous porous layer ($I = 0$) but varies for the inhomogeneity of the porous layers ($I \neq 0$). The base flow velocity profiles U_j in porous

layers depend on the inhomogeneity factor, whereas velocity U of the fluid layer is independent of inhomogeneity (\mathcal{I}). This is due to the linear form of inhomogeneity function (2.4), as it has a unit function value at the interface $y = \pm h$, i.e., $\chi_1 = \chi_2 = 1$, see (2.12). As shall see in the following subsection that the coupled linear stability equations do not depend on the base state velocity U_j of the porous layers.

2.3. Linear stability analysis

The linear stability is examined by introducing an infinitesimal disturbance in the base flow (2.11). Only two-dimensional disturbances are considered due to the Squires theorem, according to which the most unstable perturbations are two-dimensional rather than three-dimensional [35]. A temporal linear stability analysis [36, 37] is performed by introducing a normal-mode ansatz

$$\left(u, v, u_j, v_j, p, p_j\right) = \left(U, 0, U_j, 0, P, P_j\right) + \left(\widehat{u}, \widehat{v}, \widehat{u}_j, \widehat{v}_j, \widehat{p}, \widehat{p}_j\right) e^{i\alpha(x-ct)}, \quad (2.13)$$

where the hat variables are the amplitude of the disturbance; α is the real streamwise wavenumber, and c is the complex phase-speed defined as $c = c_r + ic_i$. Note that a disturbance is unstable for $\alpha c_i > 0$, stable for $\alpha c_i < 0$, and neutrally stable for $\alpha c_i = 0$. The disturbance equations are obtained by substituting (2.13) into (2.1)–(2.15) and retaining only the first-order perturbation terms in the resulting equations. Finally, the following set of linearized disturbance equations for v and v_j are achieved after eliminating pressure and horizontal velocity from the disturbance equations

$$\left[(U - c)(D^2 - \alpha^2) - (D^2 U)\right]\widehat{v} - \frac{1}{i\alpha Re} (D^2 - \alpha^2)^2 \widehat{v} = 0, \quad (2.14a)$$

$$\frac{\epsilon_j}{i\alpha Re} \left[\frac{D^2 \widehat{v}_j}{\eta_{jx}} - \xi_j \frac{\alpha^2 \widehat{v}_j}{\eta_{jy}} - \frac{D\eta_{jx} D\widehat{v}_j}{\eta_{jx}^2} \right] = c\sigma_j^2 (D^2 - \alpha^2) \widehat{v}_j, \quad (2.14b)$$

subject to the following boundary conditions

$$\widehat{v}_2 = 0 \quad \text{at } y = 1 + 2d_2, \quad (2.15a)$$

$$\widehat{v}_2 = \widehat{v} \quad \text{at } y = 1, \quad (2.15b)$$

$$D^2 \widehat{v} = \frac{\alpha_2^{BJ} (D\widehat{v} - D\widehat{v}_2)}{\sigma_2 \sqrt{\eta_{2x}(1)}} \quad \text{at } y = 1, \quad (2.15c)$$

$$\begin{aligned} -\frac{D^3 \widehat{v}}{Re} + \left(\frac{3\alpha^2}{Re} + i\alpha U\right) D\widehat{v} - i\alpha(DU)\widehat{v} - \frac{1}{\sigma_2^2 Re} \frac{D\widehat{v}_2}{\eta_{2x}(1)} \\ = i\alpha c D\widehat{v} - \frac{i\alpha c}{\epsilon_2} D\widehat{v}_2 \end{aligned} \quad \text{at } y = 1, \quad (2.15d)$$

$$\begin{aligned} -\frac{D^3 \widehat{v}}{Re} + \left(\frac{3\alpha^2}{Re} + i\alpha U\right) D\widehat{v} - i\alpha(DU)\widehat{v} - \frac{1}{\sigma_1^2 Re} \frac{D\widehat{v}_1}{\eta_{1x}(-1)} \\ = i\alpha c D\widehat{v} - \frac{i\alpha c}{\epsilon_1} D\widehat{v}_1 \end{aligned} \quad \text{at } y = -1, \quad (2.15e)$$

$$D^2 \widehat{v} = -\frac{\alpha_1^{BJ} (D\widehat{v} - D\widehat{v}_1)}{\sigma_1 \sqrt{\eta_{1x}(-1)}} \quad \text{at } y = -1, \quad (2.15f)$$

$$\widehat{v} = \widehat{v}_1 \quad \text{at } y = -1, \quad (2.15g)$$

$$\widehat{v}_1 = 0 \quad \text{at } y = -1 - 2d_1, \quad (2.15h)$$

where $D = d/dy$, $D^2 = d^2/dy^2$, $D^3 = d^3/dy^3$; \widehat{v} , \widehat{v}_2 , and \widehat{v}_1 are the amplitudes of the wall-normal velocity disturbances in the open channel layer, the upper porous and lower porous layers, respectively. For simplicity, we assume porous walls of identical heights and physical properties, i.e. $d_1 = d_2 = d$, $\epsilon_1 = \epsilon_2 = \epsilon$, $\sigma_1 = \sigma_2 = \sigma$, $\alpha_1^{BJ} = \alpha_2^{BJ} = \alpha^{BJ}$, $\xi_1 = \xi_2 = \xi$ and $\mathcal{I}_1 = \mathcal{I}_2 = \mathcal{I}$. The flow is controlled by the dimensionless parameters, namely, Re , d , σ , ϵ , α^{BJ} , ξ and \mathcal{I} .

3. Numerical method

The coupled linear stability problem (2.14) along with the boundary conditions (2.15a)–(2.15h) is solved numerically using the Chebyshev spectral collocation method [36, 38]. We approximate the disturbance amplitudes \widehat{v}_2 , \widehat{v} and \widehat{v}_1 using the Chebyshev expansions in terms of N Chebyshev polynomials as

$$\widehat{v}_2 = \sum_{n=0}^N a_n T_n(y'), \quad \widehat{v} = \sum_{n=0}^N b_n T_n(y') \quad \text{and} \quad \widehat{v}_1 = \sum_{n=0}^N c_n T_n(y'), \quad (3.1)$$

where a_n , b_n and c_n are the unknown, called Chebyshev coefficients, to be determined, and $T_n(y')$ is the n -th Chebyshev polynomial defined as

$$T_n(y') = \cos(n\theta), \quad \theta = \cos^{-1}(y'), \quad -1 \leq y' \leq 1. \quad (3.2)$$

As the Chebyshev polynomials $T_n(y')$ are defined over the domain $[-1, 1]$, the following transformation is employed to transform the physical domain $y \in [-3, 3]$ to the computational domain $y' \in [-1, 1]$

$$y' = \begin{cases} (y - d_2 - 1)/d_2 & 1 \leq y \leq 1 + 2d_2 \\ y & -1 \leq y \leq 1 \\ (y + d_1 + 1)/d_1 & -1 - 2d_1 \leq y \leq -1. \end{cases} \quad (3.3)$$

The expansions (3.1) are substituted into (2.14), and evaluated at the Gauss-Lobatto points $y_j = \cos(j\pi/N)$, which are extrema of the Chebyshev polynomials, where $j = 0, 1, 2, \dots, N$. The discretization of (2.14)–(2.15) leads to a generalized eigenvalue problem

$$\mathbf{A}X = \omega\mathbf{B}X, \quad (3.4)$$

where $\omega = \alpha c$ is the eigenvalue and X is the associated eigenvector. Equation (3.4) represents $3N + 3$ equations for the $3N + 3$ unknown Chebyshev coefficients a_j, b_j, c_j . To impose the boundary conditions, we follow Schmid and Henningson [36] and substitute the Chebyshev expansions (3.1) into (2.15). The eight boundary conditions are imposed by replacing the corresponding eight rows of \mathbf{A} and \mathbf{B} matrices of (3.4).

The corresponding disturbance amplitudes $\widehat{v} = [\widehat{v}_2, \widehat{v}, \widehat{v}_1]^T$ is found using the Chebyshev coefficients and normalized by using the maximum fluid layer velocity ($\max_{y \in [-1, 1]} |\widehat{v}|$). To check the convergence of the spectrum obtained numerically, a relative error is used as defined below

$$e_N = \frac{\|\Omega_{N+1} - \Omega_N\|_2}{\|\Omega_N\|_2}, \quad (3.5)$$

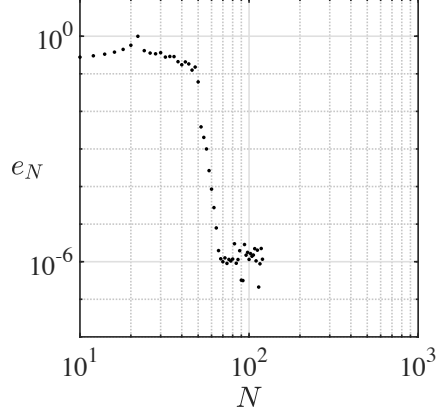


Figure 3: The variation of relative error e_N with the number N of Chebyshev polynomial in the log scale, when $Re = 2000$, $d = 1$, $\alpha = 1$, $\sigma = 0.001$, $\epsilon = 0.3$, $\alpha^{BJ} = 0.1$, $\xi = 1$ and $\mathcal{I} = 0$.

where $\|\cdot\|_2$ represents the L_2 norm, and $\mathbf{\Omega}_N$ and $\mathbf{\Omega}_{N+1}$ are vectors containing twenty least stable eigenvalues obtained using N and $N + 1$ collocation points.

Figure 3 displays the variation of relative error e_N for isotropic $\xi = 1$ and homogeneous $\mathcal{I} = 0$ porous layers as a function of collocation points N . It is seen that e_N saturates to $O(10^{-6})$ for $N \geq 70$. For other values of ξ and \mathcal{I} , similar behavior of e_N is observed (figures not presented). In addition, at $\sigma = 0.001$, the thickness ratio d has a negligible effect on the collocation points N . Therefore, $N \approx 80$ is adequate to obtain numerical accuracy at $\sigma = 0.001$.

4. Results and Discussion

The present numerical results are tested for validation with the available result of the classical plane Poiseuille flow [39]. Figure 4(a) depicts the neutral stability curve ($\omega_i = 0$) in the (α, Re) -plane for $\sigma = 10^{-5}$, with other parameters being set as $\epsilon = 0.3$, $\alpha^{BJ} = 0.1$, $\xi = 1$ and $\mathcal{I} = 0$. This set of parameters recovers stability results for classical plane Poiseuille flow. The flow is unstable ($\omega_i > 0$) inside the neutral stability curve and stable ($\omega_i < 0$) outside. The critical Reynolds number Re_c is found to be 3850, which occurs at wavenumber $\alpha_c = 1.02$. Note that the critical Reynolds number Re_c is defined as the lowest Reynolds number at which instability is triggered. Figure 4(b) depicts the eigenvalue and the eigenfunctions (inset) of the most unstable eigenvalue (marked with the red dot in the main panel) at the critical parameters $(Re_c, \alpha_c) = (3850, 1.02)$. The spectrum also shows the A , P and S branches of the classical plane Poiseuille flow [36]. It is to be noted from the eigenfunction (see the inset) of the most unstable eigenvalue that the amplitude of the perturbation velocity vanishes at the interfaces and the porous regions; thus, we recover the TS wave observed in a channel flow with impermeable walls. These results show an excellent agreement between present results with mean permeability $\sigma \approx 0$ and the classical plane Poiseuille flow.

Following previous studies [19, 40, 41], we now fix porosity, mean permeability, and Beaver-Joseph coefficient to $\epsilon = 0.3$, $\sigma = 0.001$, and $\alpha^{BJ} = 0.1$, respectively. In Secs. 4.1 and 4.2, we analyze the effect of anisotropy ξ and inhomogeneity \mathcal{I} with respect to the depth ratio d , respectively.

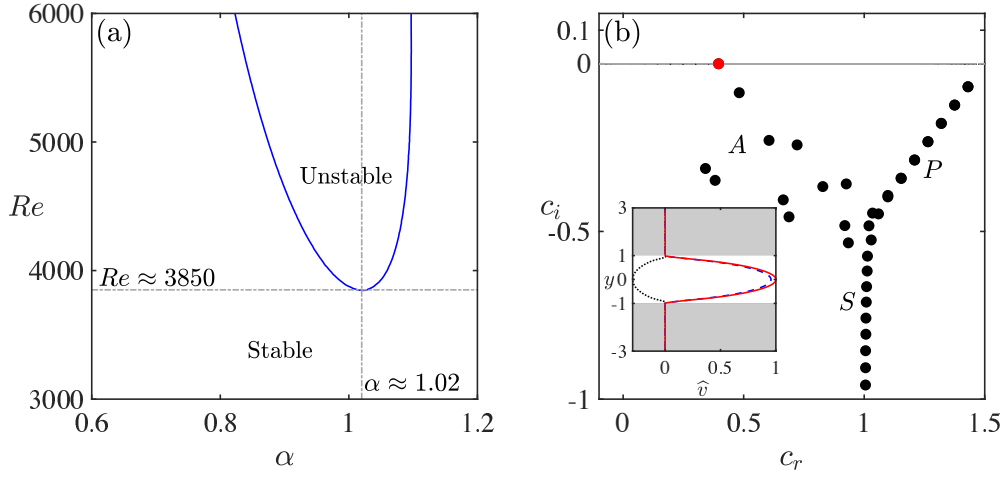


Figure 4: **(a)** The neutral stability curve in the (α, Re) -plane for $\sigma = 10^{-5}$; **(b)** Spectrum at the critical parameters $Re_c = 3850$, $\alpha_c = 1.02$. The inset shows the eigenfunction, $|\hat{v}|$ (Solid line), $\Re(\hat{v})$ (dotted line), $\Im(\hat{v})$ (dashed line), of the marked eigenvalue. The other parameters are fixed at $\epsilon = 0.3$, $\alpha^{BJ} = 0.1$, $\xi = 1$, $I = 0$.

4.1. Effect of anisotropy

This subsection studies the effect of anisotropy ξ with respect to the depth ratio d when the porous layers are homogeneous (i.e., $\eta_x = \eta_y = 1$). Figure 5 displays the anisotropy effects on

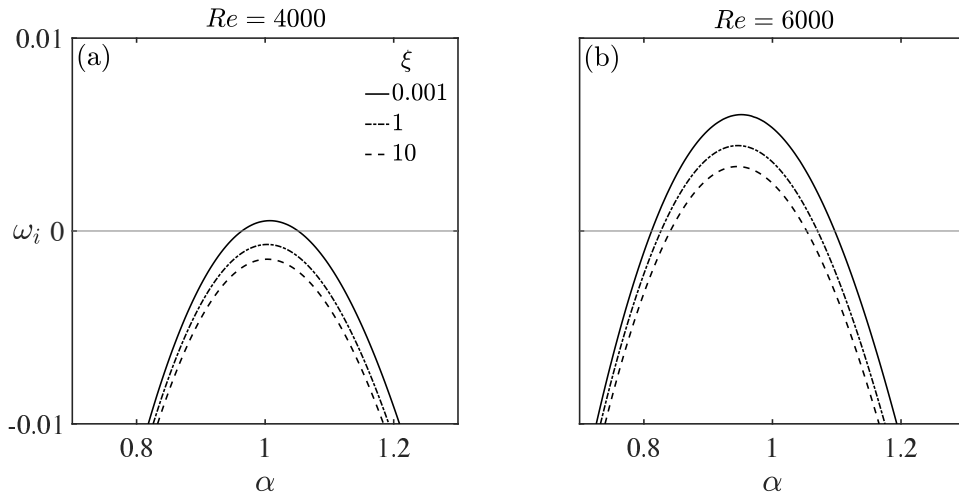


Figure 5: Variation of the growth rate ω_i with the wavenumber for $\xi = 0.001$ (solid line), 1 (dash-dotted line) and 10 (dashed line) at $d = 1$. Left and right panels represent results for (a) $Re = 4000$, and (b) $Re = 6000$.

the growth rate ω_i of the most unstable mode when $d = 1$ for two values of Reynolds number $Re = 4000$ [panel (a)] and $Re = 6000$ [panel (b)]. For both these cases, the growth rates decrease

as ξ increases for a fixed wavenumber α . The configuration remains stable when $Re = 4000$ and $\xi \geq 1$ [panel a]. Moreover, at this Re , when the relative magnitude of the cross-stream permeability is larger (i.e., $\xi = 0.001$), the growth rates become positive at wavenumber $\alpha \approx O(1)$, and the system becomes unstable. As soon as the Reynolds number Re increases to 6000, the growth rates gradually increase and become positive at each ξ [panel b]. Thus, depending on the anisotropy parameter and Reynolds number, the system destabilizes in a bandwidth of unstable wavenumbers. It is also seen from figure 5 that at fixed Re , decreasing and increasing the anisotropy parameter ξ enhances and suppresses the growth rate of the most unstable mode and, therefore, increases and decreases the bandwidth of unstable wavenumbers.

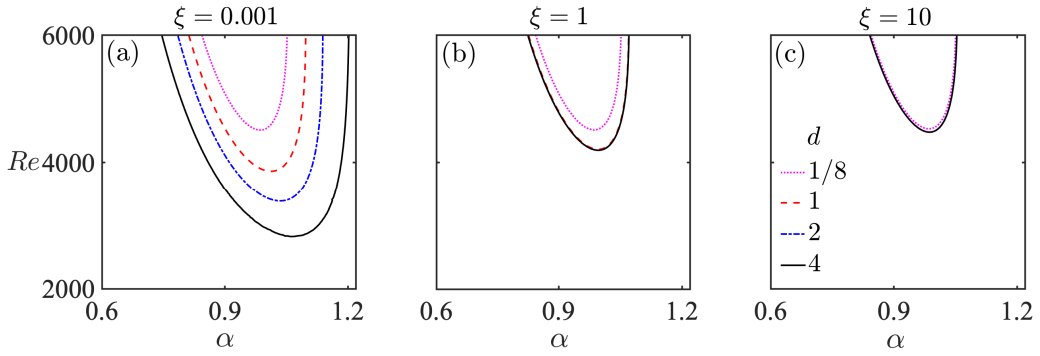


Figure 6: Neutral stability curves in (α, Re) -plane for various depth ratios d with ξ as (a) 0.001, (b) 1, and (c) 10.

To examine the effect of depth ratio d , figure 6 shows the neutral stability curves for four values of d , with the anisotropy parameter being fixed at $\xi = 0.001$ [panel a], 1 [panel b], 10 [panel c]. Note that the unstable regions become larger and the range of unstable wavenumbers increases as d increases at any fixed ξ . When $\xi \geq 1$, the neutral stability curves almost coincide, and thereby the corresponding critical Reynolds numbers are practically insensitive to the depth ratio [panels b and c]. Furthermore, at each fixed depth ratio d , the unstable region widens when the relative magnitude of the streamwise permeability is small [panel a] relative to the cross-stream permeability as against the case when the relative magnitude of the streamwise permeability are larger [panel c] relative to the cross-stream permeability. It is also evident from figure 6 that a single mode characterizes the instability domain for all ξ and d considered here. Therefore, the neutral stability curves are unimodal, similar to the classical plane Poiseuille flow [36].

d	$\xi = 0.001$		$\xi = 1$		$\xi = 10$	
	Re_c	α_c	Re_c	α_c	Re_c	α_c
1/8	4509.38	0.9864	4511.71	0.9864	4528.78	0.9862
1	3860.96	1.0109	4205.73	0.9950	4476.48	0.9870
2	3384.05	1.0340	4192.15	0.9960	4476.48	0.9860
4	2816.99	1.0570	4191.89	0.9960	4476.43	0.9860

Table 1: The effect of anisotropy parameter ξ and depth ratio d on the critical Reynolds number and critical wavenumber.

For more understanding of criticality, the critical Reynolds number Re_c and critical wavenum-

ber α_c are obtained for various ξ , and d values, and illustrated in Table 1. The table indicates that Re_c reduces by 0.052% at $\xi = 0.001$ compared to its value at $\xi = 1$ for a small depth ratio $d = 1/8$. The same trend is observed at higher $d = 4$ (reduces 32.799% for $\xi = 0.001$ compared to $\xi = 1$) when the thickness of porous layers is significantly greater than the fluid layer. However, when the relative magnitude of the streamwise permeability is greater than the relative magnitude of the cross-stream permeability, i.e., when $\xi > 1$, Re_c increases compared to the isotropic case ($\xi = 1$) for all values of depth ratio d . Particularly, for $\xi = 10$, there is an increase of 0.378% and 6.788% at $d = 1/8$ and $d = 4$, respectively.

Observe that the anisotropy parameter ξ and the depth ratio d offer a viable control technique for instability in a confined porous–fluid–porous channel. To suppress (enhance) the instability in such a system, one must design porous walls of various widths with the cross-stream permeability being smaller (more) than the streamwise permeability.

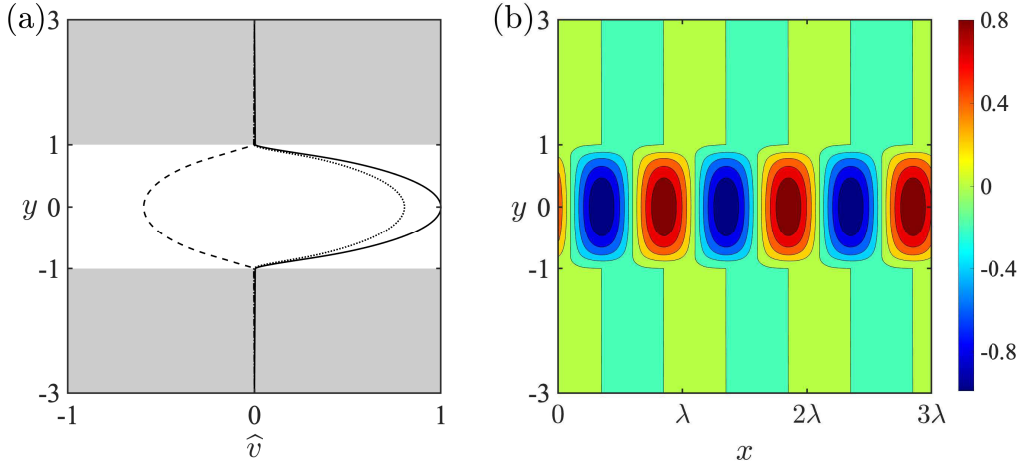


Figure 7: (a) The normalized eigenfunction, $|\widehat{v}|$ (Solid line), $\Re(\widehat{v})$ (dotted line), $\Im(\widehat{v})$ (dashed line), when $\xi = 0.001$, $Re_c = 3860.96$ and $\alpha_c = 1.0109$. (b) The contour plot of associated stream function in the (x, y) -plane. Here $\lambda = 2\pi/\alpha_c$.

It is crucial to study the dominant mode (mode with maximum growth over all wavenumbers) of instability. In this regard, the dominant instability mode at $(\alpha_c, Re_c) = (1.0109, 3860.96)$ is chosen for $\xi = 0.001$ and $d = 1$. For these parameters, the normalized eigenfunction [depicted in figure 7(a)] displays the significant variation in the open channel layer; therefore, this dominant mode is a fluid-layer mode. The corresponding contour of stream function perturbation in the (x, y) -plane is shown in figure 7(b). Here $x \in [0, 3\lambda]$ and $y \in [-1 - 2d, 1 + 2d]$, where λ represents the unit wavelength. Note that the variation of normalized eigenfunction generates a series of identically shaped vortices at the center of the open channel layer, which may be responsible for the primary instability. This fact fully supports the priority of the dominant fluid-layer mode on the primary instability, as predicted in figure 6. Similarly, for the other values of ξ and d , the dominant mode of instability has an enormous variation in the open channel-layer.

To summarize effect of anisotropy and depth ratio on the onset of instability, the variation of the critical Reynolds number Re_c and critical wavenumber α_c with the anisotropy parameter ξ for various depth ratio d are displayed in figures 8(a) and 8(b), respectively. While Re_c increases as ξ increases for all depth ratios considered here, the critical wavenumber α_c decreases with the increase in ξ . It is also seen from figure 8(a) that at a fixed depth ratio d , there is a cutoff value

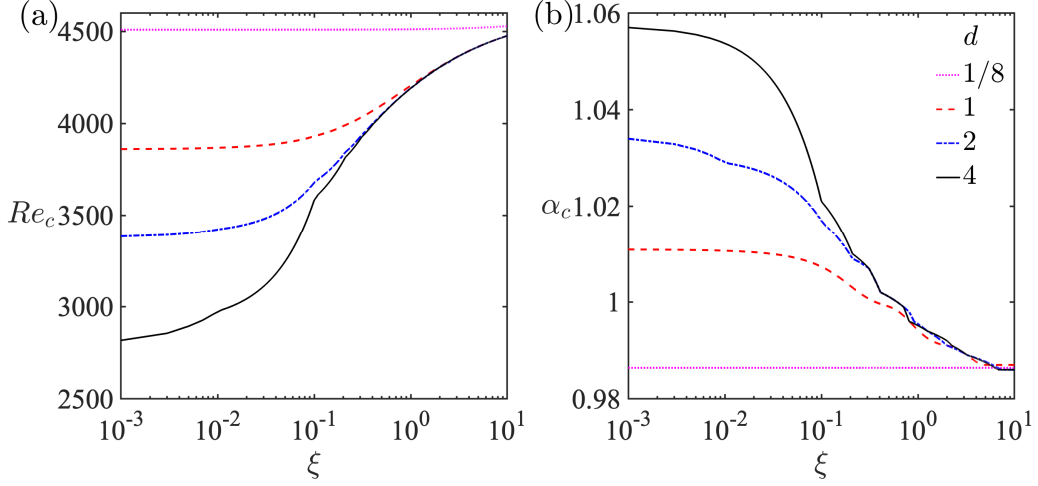


Figure 8: Variation of the (a) critical Reynolds number and (b) critical wavenumber with the anisotropy parameter ξ for various depth ratio d .

ξ_m of anisotropy parameter below which Re_c remains unchanged and above which it increases rapidly with increasing anisotropy parameter ξ ; therefore, the neutral stability curves for various $\xi \leq \xi_m$ values merge (figure not shown). Thus, the destabilizing effects of anisotropy parameter ξ are insignificant with further reduction in ξ from ξ_m . Recall that a reduction in the anisotropy parameter ξ is associated with either a relative increase in the permeability in the wall-normal direction (k_y) or a relative decrease in the permeability in the wall-parallel direction (k_x), which reduces the flow resistance, enhances the disturbance growth rate, and destabilizes the flow. The above observations reveal the significant destabilization of the system with anisotropic walls relative to the channel with porous walls as the relative magnitude of cross-stream permeability increases. Therefore, anisotropic permeability relative to isotropic permeability provides a potential strategy to control flow instability. In addition, the critical Reynolds number Re_c (the critical wavenumber α_c) decreases (increases) for each fixed ξ as d increases. As the porous layer thickness increases (decreases) relative to the fluid layer thickness, the system becomes unstable (stable), and this is true for the Poiseuille flow in a channel with either isotropic or anisotropic walls.

4.2. Effect of inhomogeneity

This subsection studies the effect of inhomogeneity \mathcal{I} concerning the depth ratio d while keeping the anisotropy parameter ξ fixed. It is worth noticing that changing \mathcal{I} is equivalent to changing the overall permeability of the porous medium. It can be seen from (2.14b) that in contrast to the anisotropy, the effect of inhomogeneity on the stability of the flow is more unpredictable since it generally appears in a complex way, as shown in this section.

Figure 9 shows the effect of the inhomogeneity factor on the growth rate of the most unstable mode when $d = 1$ for two values of the anisotropy parameter $\xi = 1$ [panel a] and $\xi = 0.001$ [panel b]. It is seen from figure 9(a) that the growth rates enhance as \mathcal{I} decrease for a fixed wavenumber α and thereby destabilizing the flow. This destabilization effect is striking for $\xi < 1$ when

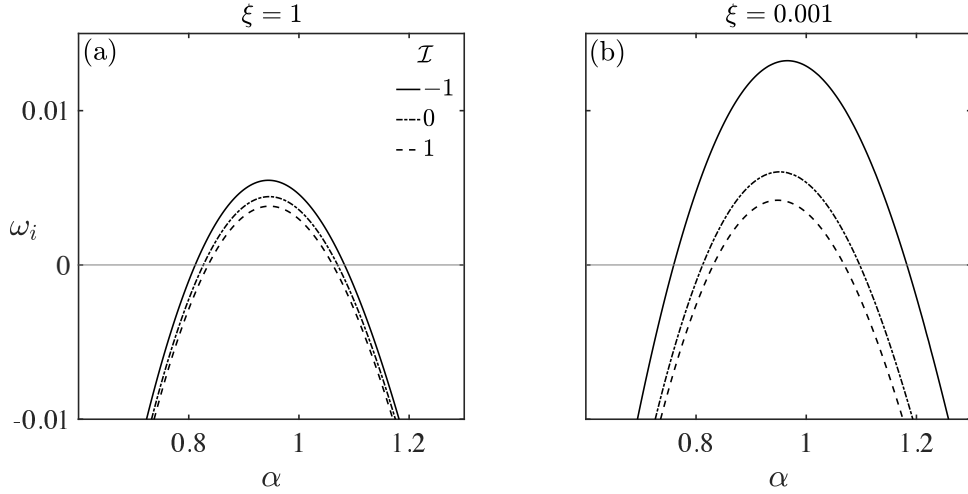


Figure 9: The temporal growth rate ω_i as a function of the wavenumber α for various values of inhomogeneity parameter \mathcal{I} ; (a) $\xi = 1$ and (b) $\xi = 0.001$. The other parameters are fixed as $Re = 6000$, $d = 1$.

inhomogeneity factor decreases, see figure 9(b). Therefore, for any fixed ξ when compared to both homogeneous ($\mathcal{I} = 0$) and inhomogeneous ($\mathcal{I} \neq 0$) porous walls, decreasing and increasing the inhomogeneity factor \mathcal{I} enhances and suppresses the growth rate of the most unstable mode, which increases and decreases the bandwidth of unstable wavenumbers.

Since the linear stability results of anisotropy parameter ξ are shown in section 4.1, we thus focus on the effect of inhomogeneity factor \mathcal{I} when $\xi = 1$ to recover inhomogeneous but isotropic porous medium. Figure 10 shows the neutral stability curves in the (α, Re) -plane for three values

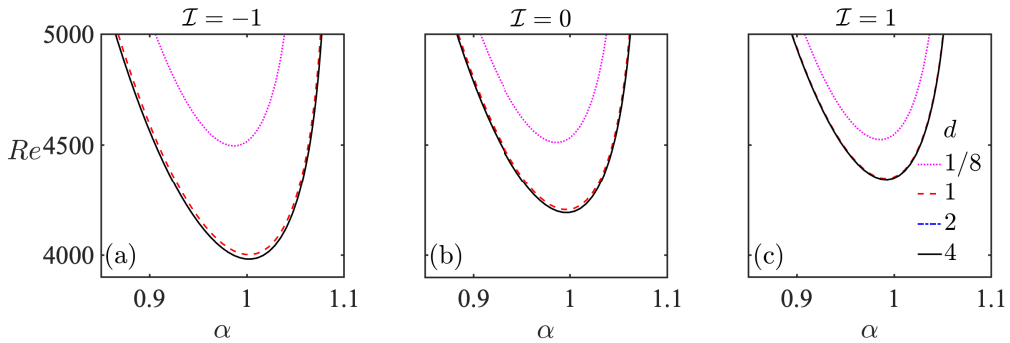


Figure 10: Neutral stability curves in the (α, Re) -plane for different values of depth ratio with $\mathcal{I} =$ (a) -1 , (b) 0 , and (c) 1 .

of inhomogeneity factor $\mathcal{I} \in \{-1, 0, 1\}$ and various values of the depth ratio d . Similar to the anisotropy, the destabilizing effect of the depth ratio continues to exist as the unstable zones expand as d increases. When $d \geq 1$, the neutral stability curves almost coincide at each \mathcal{I} , and thereby the associated critical Reynolds numbers are nearly insensitive to the depth ratio d . It is also seen from figure 10 that for each d , the unstable regions become larger, and the range of unstable wavenumbers increases as the inhomogeneity factor \mathcal{I} decreases. Similar behaviour of

stability boundaries are verified for other values of anisotropy parameter ξ .

d	$\mathcal{I} = -1$		$\mathcal{I} = 0$		$\mathcal{I} = 1$	
	Re_c	α_c	Re_c	α_c	Re_c	α_c
1/8	4469.39	0.9864	4511.71	0.9864	4524.85	0.9864
1	4001.39	1.0015	4205.73	0.9950	4348.26	0.9915
2	3981.37	1.0015	4192.15	0.9960	4344.09	0.9915
4	3981.19	1.0015	4191.89	0.9960	4344.15	0.9915

Table 2: Effect of inhomogeneity factor \mathcal{I} and depth ratio d on the critical parameters.

The critical Reynolds number Re_c and critical wavenumber α_c are obtained for various (\mathcal{I}, d) and listed in Table 2. The table indicates that Re_c reduces by 0.938% at $\mathcal{I} = -1$ compared to its value at $\mathcal{I} = 0$ (homogeneous) for a small depth ratio $d = 1/8$. The same trend is observed at higher $d = 4$ (reduces 5.026% for $\mathcal{I} = -1$ compared to $\mathcal{I} = 0$), when thickness of each porous layer is fourth times to the thickness fluid layer. However, for larger inhomogeneity factor $\mathcal{I} = 1$, there is an increase of 0.291% and 3.632% at $d = 1/8$ and $d = 4$, respectively.

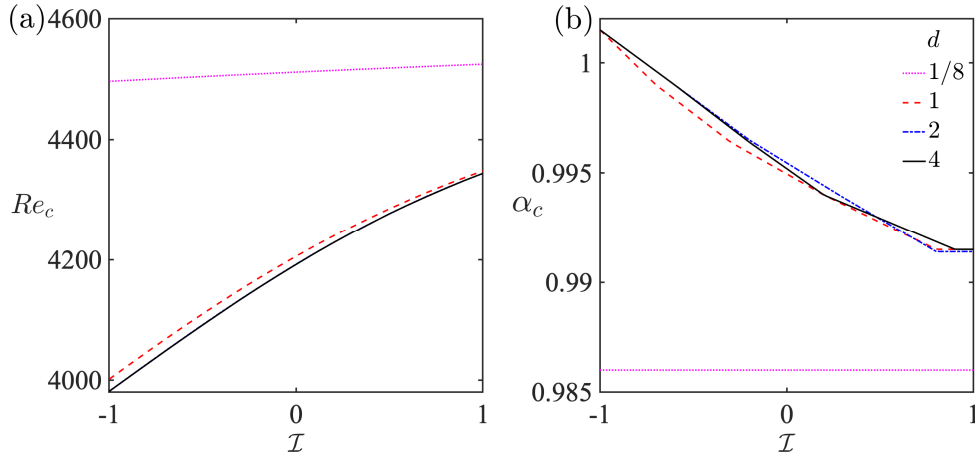


Figure 11: Variation of the (a) critical Reynolds number and (b) critical wavenumber with the inhomogeneity factor \mathcal{I} for various depth ratio d .

In the end, the variation of critical parameters Re_c and α_c with inhomogeneity factor \mathcal{I} for various depth ratios d are displayed in figures 11(a) and 11(b), respectively. Re_c (α_c) is a linear function of \mathcal{I} with a very modest slope when $d = 1/8$, i.e., for very thin porous walls. It is seen that the critical Reynolds number Re_c (critical wavenumber α_c) increases (decreases) as \mathcal{I} increases for all depth ratios considered in the present study. The above-presented results are summarized as follows. A reduction in \mathcal{I} translates to an increase in the overall permeability of the porous layers. Consequently, the flow rate increases, which reduces flow resistance, and hence flow becomes more unstable.

5. Conclusions and Outlook

Linear stability of a plane Poiseuille flow in a porous–fluid–porous configuration system with anisotropic and inhomogeneous permeability has been analyzed. The generalized Darcy’s law has been used to model the dynamics in the porous layers and Navier–Stokes equation to model the dynamics of the open fluid-layer. The base velocity has been found analytically. The linear stability of the base flow to two-dimensional infinitesimal disturbances has been analyzed. The resulting Orr–Sommerfeld eigenvalue problem has been solved numerically using the Chebyshev spectral collocation method and the QZ–algorithm. Our preliminary computations have revealed that the primary instability is triggered by the fluid-layer mode for a range of parametric values considered. Furthermore, the stability results of anisotropic and inhomogeneous permeability variation have been compared with the isotropic and homogeneous permeability. It has been found that the directional and spatial variation of permeability, i.e., anisotropy and inhomogeneity, respectively, affect the flow instability significantly. By suitably manipulating the porous walls, one can modify and control the stability characteristics of the confined porous channel flow.

The critical Reynolds number Re_c is higher (lower) with increasing (decreasing) the anisotropy parameter. Note that an increase in ξ corresponds to either a relative increase in permeability in the wall-parallel direction (k_x) or a relative decrease in permeability in the wall-normal direction (k_y). Due to a rise in ξ , the flow resistance becomes sufficiently higher, delaying the onset of instability. On the other hand, a relative increase in wall-normal permeability, i.e., decreasing ξ reduces the flow resistance, thereby advancing the onset of instability compared to a confined isotropic porous channel. It has also been found that a decrease (increase) in inhomogeneity factor \mathcal{I} , decreases (increases) the critical Reynolds number Re_c and destabilizes the flow. An inhomogeneous variation of permeability increases (decreases) the porous medium’s overall permeability and reduces (increases) the flow resistance, destabilizing (stabilizing) effects on the flow. Furthermore, present study has revealed that the channel with thicker porous walls is more unstable than the thinner porous walls.

Apart from the anisotropic and inhomogeneous permeability, and depth ratio of the porous wall in controlling the instability of the flow in a confined porous-fluid-porous, as demonstrated in the present study, there is at least one instance wherein the magnetic field acts as a control parameter. Such effects are commonly studied under *magnetohydrodynamics*. Several studies have demonstrated the stability of hydromagnetic steady flow between two parallel plates [42–45]; those are either plane Poiseuille flow, generalized Couette–Poiseuille flow, or a flow through a permeable bed. The magnetic field intensity and a decrease in porous layer permeability while flowing through a porous bed has a stabilizing effect on the fluid flow. The inclusion of the effects of the magnetic field for the present case will be considered in the future.

The present investigation motivates the experimental study to examine the instability in a pressure-driven flow in confined porous channels. However, the nonlinear analysis generally gives more significant results and will be presented in the future. The present linear stability predictions can be utilized to avoid instability in practical applications such as manufacturing composite materials. Furthermore, the results from the present study can be used to manufacture and develop smaller types of equipment required for heat exchanges where instability is desirable.

Appendix A. Linear stability results for asymmetric velocity profiles

This appendix presents the linear stability results for asymmetric velocity profiles by considering the upper porous layer as impermeable and the lower porous layer as permeable. Fig-

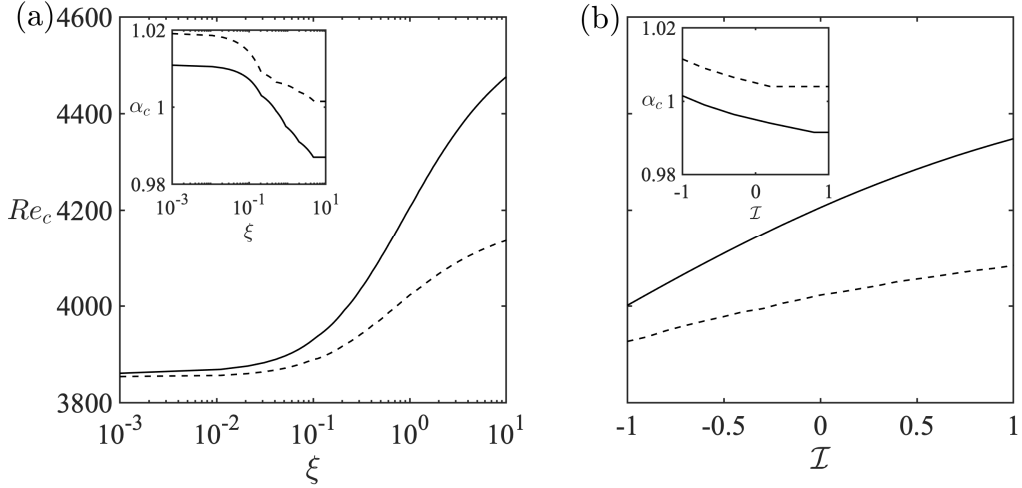


Figure A.12: Comparison of (a) the critical Reynolds number Re_c as a function of anisotropy parameter ξ when $\mathcal{I} = 0$ and (b) the critical Reynolds number Re_c as a function of inhomogeneity factor \mathcal{I} when $\xi = 1$ in a channel with two porous walls (solid line, $\sigma = 0.001$, $d = 1$) and a channel with only one porous wall (dashed line, $\sigma_1 = 0.001$, $d_1 = 1$).

ures A.12 (a) and A.12 (b) show the stability results of a channel with an impermeable upper wall and a permeable lower wall characterized by the parameters $\epsilon_1 = 0.3$, $\alpha_1^{BJ} = 0.1$, $\sigma_1 = 0.001$ and $d_1 = 1$ (dashed line), and allow for a comparison presented in figures 8 and 11 for a channel with two porous walls (solid line). Compared to a channel with two permeable homogeneous ($\mathcal{I} = 0$) porous walls, the critical Reynolds number Re_c and the critical wavenumber α_c for a homogeneous lower permeable wall are less and higher, respectively, as shown in figure A.12(a). Now, we set $\xi = 1$ and find Re_c and α_c as a function of inhomogeneity factor \mathcal{I} for a channel with two permeable porous walls and a single lower porous wall. Although the critical Reynolds number Re_c (critical wavenumber α_c) grows (decreases) with inhomogeneity factor \mathcal{I} , the critical Reynolds number Re_c (critical wavenumber α_c) for a channel with a single porous wall is smaller (larger) than a channel with two porous walls for each \mathcal{I} . From the above, it is concluded that the anisotropic and inhomogeneous permeability has less effect on the critical Reynolds number and critical wavenumber in a channel with a single porous wall than in a channel with two porous walls.

References

- [1] M. B. Allen, Collocation techniques for modeling compositional flows in oil reservoirs, Springer (1984). doi:10.1007/978-3-642-82213-1.
- [2] D. C. Blest, S. McKee, A. K. Zulkifl, P. Marshall, Curing simulation by autoclave resin infusion, Compos. Sci. Technol. (1999). doi:10.1016/S0266-3538(99)00084-6.
- [3] D. A. Nield, A. Bejan, et al., Convection in porous media, volume 3, Springer, 2006.

- [4] J. Hussong, W.-P. Breugem, J. Westerweel, A continuum model for flow induced by metachronal coordination between beating cilia, *J. Fluid Mech.* 684 (2011) 137–162. doi:10.1017/jfm.2011.282.
- [5] R. E. Ewing, S. Weekes, Numerical methods for contaminant transport in porous media, *Comput. Math.* 202 (1998) 75–95.
- [6] F. Chen, C. F. Chen, Onset of finger convection in a horizontal porous layer underlying a fluid layer, *Journal of Heat Transfer* 110 (1988) 403–409. doi:10.1115/1.3250499.
- [7] F. Chen, L. H. Hsu, Onset of thermal convection in an anisotropic and inhomogeneous porous layer underlying a fluid layer, *J. Appl. Phys.* 69 (1991) 6289–6301. doi:10.1063/1.348827.
- [8] A. Goharzadeh, A. Khalili, B. B. Jørgensen, Transition layer thickness at a fluid-porous interface, *Physics of Fluids* 17 (2005) 057102. doi:https://doi.org/10.1063/1.1894796.
- [9] B. Berkowitz, Characterizing flow and transport in fractured geological media: A review, *Advances in water resources* 25 (2002) 861–884. doi:https://doi.org/10.1016/S0309-1708(02)00042-8.
- [10] O. Makinde, Chebyshev collocation approach to stability of blood flows in a large artery, *African Journal of Biotechnology* 11 (2012) 9881–9887. doi:https://doi.org/10.5897/AJB11.3906.
- [11] N. Dukhan, Özer Bağcı, M. Özdemir, Metal foam hydrodynamics: Flow regimes from pre-darcy to turbulent, *International Journal of Heat and Mass Transfer* 77 (2014) 114–123. doi:https://doi.org/10.1016/j.ijheatmasstransfer.2014.05.017.
- [12] Z. Xiao, Y. Zhao, Heat transfer coefficient of porous copper with homogeneous and hybrid structures in active cooling, *Journal of Materials Research* 28 (2013) 2545–2553. doi:10.1557/jmr.2013.190.
- [13] J. Majdalani, C. Zhou, C. A. Dawson, Two-dimensional viscous flow between slowly expanding or contracting walls with weak permeability, *Journal of Biomechanics* 35 (2002) 1399–1403. doi:https://doi.org/10.1016/S0021-9290(02)00186-0.
- [14] H. N. Chang, J. S. Ha, J. K. Park, I. H. Kim, H. D. Shin, Velocity field of pulsatile flow in a porous tube, *Journal of Biomechanics* 22 (1989) 1257–1262. doi:https://doi.org/10.1016/0021-9290(89)90228-5.
- [15] J. J. Voermans, M. Ghisalberti, G. N. Ivey, The variation of flow and turbulence across the sediment–water interface, *Journal of Fluid Mechanics* 824 (2017) 413–437. doi:10.1017/jfm.2017.345.
- [16] Y. Kuwata, K. Suga, Direct numerical simulation of turbulence over anisotropic porous media, *Journal of Fluid Mechanics* 831 (2017) 41–71. doi:10.1017/jfm.2017.619.
- [17] M. E. Rosti, L. Brandt, A. Pinelli, Turbulent channel flow over an anisotropic porous wall – drag increase and reduction, *Journal of Fluid Mechanics* 842 (2018) 381–394. doi:10.1017/jfm.2018.152.
- [18] Chang, Min-Hsing, Chen, Falin, S. Brian, Instability of poiseuille flow in a fluid overlying a porous layer, *J. Fluid Mech.* 564 (2006) 287–303. doi:10.1017/S0022112006001583.
- [19] R. Liu, Q. S. Liu, S. C. Zhao, Instability of plane poiseuille flow in a fluid-porous system, *Phys. Fluid* 20 (2008) 104105. doi:10.1063/1.3000643.
- [20] A. A. Hill, B. Straughan, Poiseuille flow in a fluid overlying a porous medium, *J. Fluid Mech.* 603 (2008) 137–149. doi:10.1017/S0022112008000852.
- [21] N. Tilton, L. Cortelezzi, The destabilizing effects of wall permeability in channel flows: A linear stability analysis, *Phys. Fluid* 18 (2006) 051702. doi:10.1063/1.2202649.
- [22] N. Tilton, L. Cortelezzi, Linear stability analysis of pressure-driven flows in channels with porous walls, *J. Fluid Mech.* 604 (2008) 411–445. doi:10.1017/S0022112008001341.
- [23] S. Whitaker, The forchheimer equation: a theoretical development, *Trans. Porous media* 25 (1996) 27–61. doi:10.1007/BF00141261.
- [24] J. A. Ochoa-Tapia, S. Whitaker, Momentum transfer at the boundary between a porous medium and a homogeneous fluid—i. theoretical development, *Int. J. Heat Mass Transfer* 38 (1995) 2635–2646. doi:10.1016/0017-9310(94)00346-w.
- [25] J. A. Ochoa-Tapia, S. Whitaker, Momentum transfer at the boundary between a porous medium and a homogeneous fluid—II. comparison with experiment, *Int. J. Heat Mass Transfer* 38 (1995) 2647–2655. doi:10.1016/0017-9310(94)00347-x.
- [26] B. Straughan, *Stability and wave motion in porous media*, volume 165, Springer Science & Business Media, 2008. doi:https://doi.org/10.1007/978-0-387-76543-3.
- [27] B. Straughan, D. Walker, Anisotropic porous penetrative convection, *Proc. R. Soc. Lond. Series A* 452 (1996) 97–115. doi:10.1098/rspa.1996.0006.
- [28] M. Malashetty, M. Swamy, The onset of convection in a binary fluid saturated anisotropic porous layer, *Int. J. Thermal Sc.* 49 (2010) 867–878. doi:10.1016/j.ijthermalsci.2009.12.008.
- [29] P. Deepu, P. Anand, S. Basu, Stability of poiseuille flow in a fluid overlying an anisotropic and inhomogeneous porous layer, *Phys. Rev. E* 92 (2015) 023009. doi:10.1103/PhysRevE.92.023009.
- [30] G. S. Beavers, D. D. Joseph, Boundary conditions at a naturally permeable wall, *J. Fluid Mech.* 30 (1967) 197–207. doi:10.1017/S0022112067001375.
- [31] T. Green, R. L. Freehill, Marginal stability in inhomogeneous porous media, *Journal of Applied Physics* 40 (1969)

- 1759–1762. doi:<https://doi.org/10.1063/1.1657844>.
- [32] F. Chen, Salt-finger instability in an anisotropic and inhomogeneous porous substrate underlying a fluid layer, *Journal of applied physics* 71 (1992) 5222–5236. doi:<https://doi.org/10.1063/1.350579>.
- [33] P. Deepu, S. Dawande, S. Basu, Instabilities in a fluid overlying an inclined anisotropic and inhomogeneous porous layer, *Journal of Fluid Mechanics* 762 (2015) R2. doi:10.1017/jfm.2014.644.
- [34] B. Goyeau, D. Lhuillier, D. Gobin, M. Velarde, Momentum transport at a fluid–porous interface, *Int. J. Heat Mass Transfer* 46 (2003) 4071–4081. doi:10.1016/S0017-9310(03)00241-2.
- [35] H. B. Squire, On the stability for three-dimensional disturbances of viscous fluid flow between parallel walls, *Proceedings of the Royal Society of London. Series A, Containing Papers of a Mathematical and Physical Character* 142 (1933) 621–628. doi:10.1098/rspa.1933.0193.
- [36] P. J. Schmid, D. S. Henningson, *Stability and transition in shear flows*, Springer (2001). doi:10.1007/978-1-4613-0185-1.
- [37] P. G. Drazin, W. H. Reid, *Hydrodynamic stability*, Cambridge university press, 2004.
- [38] C. Canuto, M. Hussaini, A. M. Quarteroni, T. A. Zang, *Spectral Methods in Fluid Dynamics*, Springer-Verlag, Berlin, 1988.
- [39] S. A. Orszag, Accurate solution of the orr–sommerfeld stability equation, *Journal of Fluid Mechanics* 50 (1971) 689–703. doi:10.1017/S0022112071002842.
- [40] M.-H. Chang, F. Chen, B. Straughan, Instability of poiseuille flow in a fluid overlying a porous layer, *Journal of Fluid Mechanics* 564 (2006) 287–303. doi:10.1017/S0022112006001583.
- [41] M.-H. Chang, Thermal convection in superposed fluid and porous layers subjected to a plane poiseuille flow, *Physics of Fluids* 18 (2006) 035104. doi:10.1063/1.2182004.
- [42] O. Makinde, Magneto-hydrodynamic stability of plane-poiseuille flow using multi-deck asymptotic technique, *Mathematical and Computer Modelling* 37 (2003) 251–259. doi:[https://doi.org/10.1016/S0895-7177\(03\)00004-9](https://doi.org/10.1016/S0895-7177(03)00004-9).
- [43] O. Makinde, P. Mhone, Temporal stability of small disturbances in mhd jeffery–hamel flows, *Computers & Mathematics with Applications* 53 (2007) 128–136. doi:<https://doi.org/10.1016/j.camwa.2006.06.014>.
- [44] O. D. Makinde, P. Mhone, On temporal stability analysis for hydromagnetic flow in a channel filled with a saturated porous medium, *Flow, Turbulence and Combustion* 83 (2009) 21–32. doi:<https://doi.org/10.1007/s10494-008-9187-6>.
- [45] O. Makinde, S. Motsa, Hydromagnetic stability of generalized plane couette flow, *Far East J. Appl. Math* 6 (2002) 77–88.